Comparison of POD-UDEIM and POD-ECSW model order reduction in the case of damaging RC structures subjected to earthquakes

Bastien Bodnar, Walid Larbi, Magdalini Titirla, Jean-François Deü, Fabrice Gatuingt, Frédéric Ragueneau

COMPDYN 2023
9th ECCOMAS Thematic Conference on
Computational Methods in Structural Dynamics and Earthquake Engineering
M. Papadrakakis, M. Fragiadakis (eds.)
Athens, Greece, 12-14 June 2023

COMPARISON OF POD-UDEIM AND POD-ECSW MODEL ORDER REDUCTION IN THE CASE OF DAMAGING RC STRUCTURES SUBJECTED TO EARTHQUAKES

B. Bodnar[1, 2], W. Larbi[1], M. Titirla[1], J.-F. Deü[1], F. Gatuingt[2] and F. Ragueneau[2, 3]

[1] Conservatoire National des Arts et Métiers, Laboratoire de Mécanique des Structures et des Systèmes Couplés
292 rue Saint-Martin, 75141 Paris cedex 03, France
{bastien.bodnar, walid.larbi, magdalini.titirla, jean-francois.deu}@lecnam.net

[2] Université Paris-Saclay, Centrale Supélec, ENS Paris-Saclay, CNRS, Laboratoire de Mécanique Paris-Saclay
91190, Gif-sur-Yvette, France
{bastien.bodnar, fabrice.gatuingt, frederic.ragueneau}@ens-paris-saclay.fr

[3]EPF École d'Ingénieurs
{frederic.ragueneau}@epf.fr
55 av. Président Wilson, F-94230, Cachan, France

Abstract

This paper uses Hyper-Reduced Order Models (HROMs) to accelerate parametric and sensitivity analyses on reinforced concrete structures subjected to earthquakes. The number of Degrees Of Freedom (DOFs) is reduced using a Proper Orthogonal Decomposition (POD) reduced basis. The nonlinear terms of the matrix system are approximated using an Unassembled Discrete Empirical Interpolation Method (UDEIM) or an Energy Conserving with Sampling and Weighting procedure (ECSW). Both strategies are compared regarding accuracy and time-savings on a L-shaped three-story building modeled by damaging multifibre beam elements. The efficiency of the HROMs is assessed in the case of parametric analyses about the external loading (e.g., ground motions) or mechanical properties (e.g., elastic modulus, or tensile strength). Results (1) show that both methods correctly model the nonlinear response of the structure with a strain energy error of less than 0.5 % and a speed-up factor between 20 and 32 during the online phases, and (2) prove that the POD-ECSW is more accurate than the POD-UDEIM despite an offline phase that requires more CPU time.

Keywords: Earthquake Engineering, Reinforced Concrete, Multifibre Beam Elements, Model Order Reduction, Proper Orthogonal Decomposition, Unassembled Discrete Empirical Interpolation Method, Energy Conserving with Sampling and Weighting.

1 INTRODUCTION

An important part of Reinforced Concrete (RC) structures design is the capability to withstand dynamic loadings (e.g., earthquakes, or wind). Accurately assessing such structural responses requires 3D nonlinear dynamic Finite Element (FEM) analyses. However, it is not easy since it can be costly in Central Processing Unit (CPU) time. As a result, knowing that FEM analyses usually do not exceed 12 hours in a civil engineering design office, other approaches are used instead for design purposes. Among them, the widespread quasi-static "push-over" method allows computing the loading demand on each structural component (e.g., column, or beam) for several earthquakes without performing dynamic FEM analyses ([1], [2]). This approach is well suited for design but is limited compared to dynamic FEM analyses since the higher eigenmodes and the earthquake-induced cyclic loading are not considered. As a result, torsional effects or local collapse mechanisms cannot be modeled correctly, as well as hysteretic energy dissipations (e.g., frictional sliding) or stiffness recovery when the cracks are closing. To consider all these phenomena, nonlinear dynamic FEM analyses must be repeated with several ground motions coming from one or several directions. Reducing the computational cost of such sensitivity analyses is thus useful in an industrial context. The development of pseudo-dynamic and real-time hybrid tests over the last decades also pushed forward the need for nonlinear numerical models of RC structures that can be run in quasi-real time ([3], [4]). As the commands of the actuators are based on the response of a nonlinear numerical model, the CPU time must be less than 10 ms per time step in real-time. Lower values can sometimes be required depending on the delays related to the components of the experimental setup (e.g., actuators, sensors, or controller boards). Hyper-Reduced Order Models (HROMs) can be used to reach these goals.

In the case of nonlinear systems, *a posteriori* data-driven methods are commonly applied. Training FEM analyses are first run on the nonlinear high dimensional system to generate relevant snapshots. Offline post-processing is then carried out to produce modes that best represent the nonlinear response of the model. The modal basis can be computed using a "greedy" fixed point algorithm or a Proper Orthogonal Decomposition (POD) method to build orthogonal modes incrementally or simultaneously ([5], [6], [7]). Several researchers successfully used the POD over the last decades to identify coherent structures [8], perform FEM analyses involving turbulent flows ([9], [10]), control dynamic systems [11], detect damage [12], update finite element models [13], and reduce structural dynamics models ([14], [15]). This approach drastically reduces the computational cost required to solve nonlinear matrix systems. However, it is limited since the computational cost related to the nonlinear terms (e.g., restoring forces) is still very high.

Using hyper-reduction methods avoids this drawback. They consist of approximating the nonlinear terms based on samples assessed on a set of elements belonging to a Reduced Integration Domain (RID). The Discrete Empirical Interpolation Method (DEIM) and its variants allow for achieving this purpose [16]. They rely on the "gappy" POD used to reconstruct facial images [17], hyper-reduce nonlinear systems in the fluid dynamics framework ([18], [19]), or perform process simulations [20]. DEIM approaches can be seen as an improvement of this method since a "greedy" algorithm is added to the offline phase to identify the best RID. As it is used with the POD to perform FEM analyses, no additional CPU time is required to build force snapshots. The procedure also remains the same regardless of the physics since the snapshots consider all the nonlinearities (e.g., damage, plasticity, or large deformations). Several collocation techniques allow using all the components belonging to the RID, improving the stability and the accuracy of the HROM [21]. The unassembled force snapshots (i.e., computed

element per element) can also be used to build the force basis [22]. As each collocation component refers to an element instead of a node, the elements belonging to the RID are directly selected when the greedy algorithm runs, making the unassembled DEIM (UDEIM) more suitable to perform FEM analyses. Better accuracy can thus be reached with smaller RIDs [21]. Other improvements were developed over the last decade, such as a localized DEIM ([23], [24]), an adaptation to parametric systems ([25], [26]), improved strategies to choose the collocation components [27], or applications to geometrically nonlinear static and dynamic systems involving nonlinear elastic material laws ([28], [21]). The DEIM and its variants are efficient but come with a huge drawback since they destroy the symmetry of the matrix system. The approximated DEIM reduced tangent operator is not entirely symmetric, which leads to a possible loss of stability, variational consistency, and underlying energy function fitting into the Lagrangian framework [21]. As a result, only the nonlinear part of the nonlinear terms can be interpolated. Other approaches, such as the Energy Conserving Mesh Sampling and Weighting (ECSW), need to be used instead to keep the symmetry of the matrix system. It consists of finding the smallest number of positive non-null weights applied to a reduced set of elements (belonging to the RID) so that the sum of their contribution is equal to the reduced restoring force vector up to a tolerance usually lower than 1 %. Contrary to the DEIM, the nonlinear terms are directly approximated on a reduced basis. The contribution of each element is computed separately according to the available unassembled force snapshots. A greedy Sparse Non-Negative Least Square (SNNLS) solver is then used during the offline phase to compute the weights applied to the elements belonging to the RID. The ECSW was initially developed in the framework of computer graphics [29] and later extended to the finite element framework to solve structural dynamics problems ([30], [31]). Several researchers worked later on improvements to reduce the computational cost due to the sparse SNNLS solver [32], or to selectively evaluate the nonlinearities at the Gauss point level instead of the element scale [33]. The ECSW proved to be more efficient than the DEIM approaches in the case of dynamic FEM analyses involving geometrical nonlinearities and nonlinear elastic materials [21].

This paper uses hyper-reduction methods to accelerate earthquake engineering parametric and sensitivity analyses on a reinforced concrete structure. To do so, both UDEIM and ECSW are compared in terms of accuracy and time-saving. The POD and the UDEIM procedures are detailed in Section 2, while the ECSW is described in Section 3. Hyper-reduced models are used in Section 4 to accelerate parametric analyses about the external loading (i.e., ground motion) and material properties (i.e., elastic modulus, tensile strength, and compressive strength of concrete) on a L-shaped three-story building made of multi-fiber beam elements.

2 REDUCED ORDER MODELING USING A POD-UDEIM APPROACH

Using nonlinear material laws increases the CPU time necessary to compute the nonlinear restoring force vector at each time step. In addition, performing all the matrix operations on a full basis can be time-consuming, especially if the structure has many DOFs. To reduce the computational cost of the Full Order Model (FOM), a POD-UDEIM hyper-reduced order modeling approach is proposed.

The key idea of the POD is to first perform a small number of nonlinear FEM analyses (e.g., by using earthquakes having different peak ground accelerations, frequency, strong motion phase duration, or oriented in different directions) on the FOM made of N_{DOFs} free DOFs. Displacement snapshots are then used as training data to compute N nonlinear POD modes by carrying out a Singular Value Decomposition (SVD). The n first POD modes are next selected according to the criterion (1) to build a reduced modal basis:

$$1 - \frac{\sum_{i=1}^{n} \lambda_i}{\sum_{j=1}^{N} \lambda_j} \leq \varepsilon \tag{1}$$

where λ_i is the i^{th} singular value, N is the number of POD modes, $n \ll N$ is the number of POD modes in the truncated modal basis, and ε is the tolerance used to truncate the modal basis.

A tolerance ε of 10^{-2} is recommended to ensure that approximately 99 % of the data quantified by the singular values is considered in the POD basis [15]. This *a posteriori* approach reduces the number of DOFs as well as the computational cost of the matrix operations. The displacement vector $\boldsymbol{u} \in \mathbb{R}^{N_{DOFs}}$ can thus be expressed in a new basis $\boldsymbol{\Phi} \in \mathbb{R}^{N_{DOFs} \times n}$ as described in (2):

$$\boldsymbol{u} \approx \boldsymbol{\Phi} \cdot \boldsymbol{q} \qquad \text{with} \qquad \boldsymbol{\Phi} = [\boldsymbol{\varphi}_1 \quad \cdots \quad \boldsymbol{\varphi}_n] \tag{2}$$

where $\boldsymbol{q} \in \mathbb{R}^n$ is the displacement vector in the reduced basis $\boldsymbol{\Phi}$, and $\boldsymbol{\varphi}_{i=1,\dots,n} \in \mathbb{R}^{N_{DOFs}}$ is the i^{th} POD mode computed using a SVD procedure.

In addition, a UDEIM operator is added to the solving process. To do so, a second SVD is performed on the snapshots related to the nonlinear parts of the unassembled restoring force vector (i.e., computed element per element) (3). N_e is the number of finite elements, and N_c is the number of force components per element:

$$\boldsymbol{r}^{\mathrm{NL,u}}(\boldsymbol{u}) = \boldsymbol{r}^{\mathrm{u}}(\boldsymbol{u}) - \boldsymbol{K}_{\mathrm{E}}^{\mathrm{u}} \cdot \boldsymbol{B} \cdot \boldsymbol{u} \tag{3}$$

where $\boldsymbol{K}_{\mathrm{E}}^{\mathrm{u}} \in \mathbb{R}^{N_e \cdot N_c \times N_e \cdot N_c}$ is the unassembled elastic stiffness matrix, $\boldsymbol{B} = \left[\boldsymbol{L}_1^T \quad \cdots \quad \boldsymbol{L}_{N_e}^T\right]^T \in \mathbb{R}^{N_e \cdot N_c \times N_{DOFs}}$ is a Boolean assembly matrix, and $\boldsymbol{L}_{i=1,\dots,N_e} \in \mathbb{R}^{N_c \times N_{DOFs}}$ is a collocation matrix used to select the displacements of the nodes connected to the i^{th} finite element (4):

$$\boldsymbol{r}^{\mathrm{u}} = \begin{pmatrix} \boldsymbol{r}_1^{\mathrm{u}} \\ \vdots \\ \boldsymbol{r}_{N_e}^{\mathrm{u}} \end{pmatrix} \quad \& \quad \boldsymbol{K}_{\mathrm{E}}^{\mathrm{u}} = \begin{pmatrix} \boldsymbol{K}_{\mathrm{E},1}^{\mathrm{u}} & \dots & \boldsymbol{0} \\ \vdots & \ddots & \vdots \\ \boldsymbol{0} & \dots & \boldsymbol{K}_{\mathrm{E},N_e}^{\mathrm{u}} \end{pmatrix}. \tag{4}$$

The m first UDEIM modes are then selected according to (1) to build a second truncated modal basis $\boldsymbol{\Psi} \in \mathbb{R}^{N_e \cdot N_c \times m}$. So $\boldsymbol{r}^{\mathrm{NL,u}} \cong \boldsymbol{\Psi} \cdot \boldsymbol{c}$ where $\boldsymbol{c} \in \mathbb{R}^m$ is the vector containing the scalar weights associated with the truncated modal basis $\boldsymbol{\Psi} = [\boldsymbol{\psi}_1 \quad \cdots \quad \boldsymbol{\psi}_m]$. Algorithm 1 is next used to find for each UDEIM mode $\boldsymbol{\psi}_i \in \mathbb{R}^{N_e \cdot N_c}$ the best collocation component.

Algorithm 1: DEIM algorithm.

Input: A set of DEIM modes $\boldsymbol{\Psi} = [\boldsymbol{\psi}_1 \quad \cdots \quad \boldsymbol{\psi}_m]$
Output: Index of the interpolation DOFs $\boldsymbol{ID} = [ID_1 \quad \cdots \quad ID_m]$ and partition matrix $\boldsymbol{P} = [\boldsymbol{p}_1 \quad \dots \quad \boldsymbol{p}_m]$

Set ID_1 = index of the maximum component of $|\boldsymbol{\psi}_1|$
Set $\boldsymbol{I}_d = [\boldsymbol{e}_1 \quad \dots \quad \boldsymbol{e}_{N_e \cdot N_c}]$ the identity matrix of size $N_e \cdot N_c \times N_e \cdot N_c$
Initiate matrices : $\boldsymbol{V} = [\boldsymbol{\psi}_1]$, $\boldsymbol{P} = \left[\boldsymbol{e}_{ID_1}\right]$, $\boldsymbol{ID} = [ID_1]$

For $i = 2, \dots, m$ do
  Solve $\boldsymbol{P}^{\mathrm{T}} \cdot \boldsymbol{V} \cdot \boldsymbol{c}_i = \boldsymbol{P}^{\mathrm{T}} \cdot \boldsymbol{\psi}_i$
  Compute residual $\boldsymbol{res} = |\boldsymbol{\psi}_i - \boldsymbol{V} \cdot \boldsymbol{c}_i|$
  Set ID_i = index of the maximum component of $\boldsymbol{res}$
  Augment $\boldsymbol{V} \leftarrow [\boldsymbol{V} \quad \boldsymbol{\psi}_i]$, $\boldsymbol{P} \leftarrow [\boldsymbol{P} \quad \boldsymbol{e}_{ID_i}]$, $\boldsymbol{ID} \leftarrow [\boldsymbol{ID} \quad ID_i]$
End

The m components belonging to the RID are selected using a Boolean partition matrix $\boldsymbol{P} \in \mathbb{R}^{N_e \cdot N_c \times m}$. To improve the accuracy of the interpolation operator, the unused components of the RID are added to $\boldsymbol{P}$. The number of collocation components k is thus higher than the number m of UDEIM modes (i.e., $k > m$). Considering a new partition matrix $\boldsymbol{P} \in \mathbb{R}^{N_e \cdot N_c \times k}$ leads to an overdetermined matrix system $\boldsymbol{P}^{\mathrm{T}} \cdot \boldsymbol{\psi} \cdot \boldsymbol{c} \approx \boldsymbol{P}^{\mathrm{T}} \cdot \boldsymbol{r}^{\mathrm{NL,u}}$. The scalar weights $\boldsymbol{c} \in \mathbb{R}^m$ are thus computed in the least square sense using a Monroe-Penrose pseudo-inverse $(\cdot)^+$ so that the residual is minimized in the L^2-norm, leading to $\boldsymbol{c} \approx (\boldsymbol{P}^{\mathrm{T}} \cdot \boldsymbol{\psi})^+ \cdot \boldsymbol{P}^{\mathrm{T}} \cdot \boldsymbol{r}^{\mathrm{NL,u}}$. It should be noted that the selection of the collocation components could be improved by directly adding the additional components to $\boldsymbol{P}$ when Algorithm 1 runs [21]. Unfortunately, the CPU time related to the offline phase drastically increases since the size of the matrix system to solve at each iteration is N_c times higher. In addition, the accuracy of the interpolation operator does not change significantly. As a result, the additional components are here added to $\boldsymbol{P}$ *a posteriori* (i.e., when the RID is already defined).

When the k collocation components are set, the online phases proceed. The material laws are only updated on the elements belonging to the RID (i.e., where the nonlinear part of the unassembled restoring force vector needs to be computed). The k collocation components stored in $\boldsymbol{r}_{\mathrm{RID}}^{\mathrm{NL,u}} = \boldsymbol{P}^{\mathrm{T}} \cdot \boldsymbol{r}^{\mathrm{NL,u}} \in \mathbb{R}^k$ are then used as samples to build the reduced vector $\overline{\boldsymbol{r}} \in \mathbb{R}^n$ in basis $\boldsymbol{\Phi}$, as described in (5):

$$\overline{\boldsymbol{r}}(\boldsymbol{\Phi} \cdot \boldsymbol{q}) = \boldsymbol{\Phi}^{\mathrm{T}} \cdot \boldsymbol{B}^{\mathrm{T}} \cdot \left(\boldsymbol{K}_{\mathrm{E}}^{\mathrm{u}} \cdot \boldsymbol{B} \cdot \boldsymbol{\Phi} \cdot \boldsymbol{q} + \boldsymbol{A} \cdot \boldsymbol{r}_{\mathrm{RID}}^{\mathrm{NL,u}}(\boldsymbol{\Phi} \cdot \boldsymbol{q}) \right) \quad \text{with} \quad \boldsymbol{A} = \boldsymbol{\Psi} \cdot (\boldsymbol{P}^{\mathrm{T}} \cdot \boldsymbol{\Psi})^+ \tag{5}$$

where $\boldsymbol{K}_{\mathrm{E}}^{\mathrm{u}} \in \mathbb{R}^{N_e \cdot N_c \times N_e \cdot N_c}$ is the unassembled elastic stiffness matrix, $\boldsymbol{\Phi} \in \mathbb{R}^{N_{DOFs} \times n}$ is the basis of POD modes, $\boldsymbol{q} \in \mathbb{R}^n$ is the displacement vector in basis $\boldsymbol{\Phi}$, $\boldsymbol{\Psi} \in \mathbb{R}^{N_e \cdot N_c \times m}$ is the basis of UDEIM modes, $\boldsymbol{P} \in \mathbb{R}^{N_e \cdot N_c \times k}$ is the partition matrix, and $\boldsymbol{A} \in \mathbb{R}^{N_e \cdot N_c \times k}$ is the UDEIM interpolation operator. As a result, according to (3), (5) becomes:

$$\overline{\boldsymbol{r}}(\boldsymbol{\Phi} \cdot \boldsymbol{q}) = \boldsymbol{\Phi}^{\mathrm{T}} \cdot \boldsymbol{B}^{\mathrm{T}} \cdot \left((\boldsymbol{I}_{\mathrm{d}} - \boldsymbol{A} \cdot \boldsymbol{P}^{\mathrm{T}}) \cdot \boldsymbol{K}_{\mathrm{E}}^{\mathrm{u}} \cdot \boldsymbol{B} \cdot \boldsymbol{\Phi} \cdot \boldsymbol{q} + \boldsymbol{A} \cdot \boldsymbol{r}_{\mathrm{RID}}^{\mathrm{u}}(\boldsymbol{\Phi} \cdot \boldsymbol{q}) \right) \tag{6}$$

where $\boldsymbol{I}_{\mathrm{d}} \in \mathbb{R}^{N_e \cdot N_c \times N_e \cdot N_c}$ is an identity matrix, and $\boldsymbol{r}_{\mathrm{RID}}^{\mathrm{u}}(\boldsymbol{\Phi} \cdot \boldsymbol{q}) \in \mathbb{R}^k$ is the unassembled restoring force vector assessed on the k collocation components belonging to the RID. The reduced tangent stiffness matrix $\overline{\boldsymbol{K}}_{\mathrm{T}} \in \mathbb{R}^{n \times n}$ can thus be approximated by derivation of (6) with respect to $\boldsymbol{q}$ (7):

$$\overline{\boldsymbol{K}}_{\mathrm{T}} = \frac{\partial \overline{\boldsymbol{r}}(\boldsymbol{q})}{\partial \boldsymbol{q}} \approx \boldsymbol{\Phi}^{\mathrm{T}} \cdot \boldsymbol{B}^{\mathrm{T}} \cdot \left((\boldsymbol{I}_{\mathrm{d}} - \boldsymbol{A} \cdot \boldsymbol{P}^{\mathrm{T}}) \cdot \boldsymbol{K}_{\mathrm{E}}^{\mathrm{u}} + \boldsymbol{A} \cdot \boldsymbol{K}_{\mathrm{T,RID}}^{\mathrm{u}} \right) \cdot \boldsymbol{B} \cdot \boldsymbol{\Phi} \tag{7}$$

where $\boldsymbol{K}_{\mathrm{T,RID}}^{\mathrm{u}} = \frac{\partial \boldsymbol{r}_{\mathrm{RID}}^{\mathrm{u}}(\boldsymbol{\Phi} \cdot \boldsymbol{q})}{\partial \boldsymbol{B} \cdot \boldsymbol{\Phi} \cdot \boldsymbol{q}} = \boldsymbol{P}^{\mathrm{T}} \cdot \frac{\partial \boldsymbol{r}^{\mathrm{u}}(\boldsymbol{\Phi} \cdot \boldsymbol{q})}{\partial \boldsymbol{B} \cdot \boldsymbol{\Phi} \cdot \boldsymbol{q}} \in \mathbb{R}^{k \times N_e \cdot N_c}$ is the unassembled tangent stiffness matrix related to the k collocation components belonging to the RID, computed when iterating and used as a sample to approximate $\overline{\boldsymbol{K}}_{\mathrm{T}}$ during the online phase.

3 REDUCED ORDER MODELING USING A POD-ECSW APPROACH

The ECSW is a hyper-reduction method that preserves the virtual work of the reduced restoring force vector $\overline{\boldsymbol{r}}(\boldsymbol{\Phi} \cdot \boldsymbol{q}) \in \mathbb{R}^n$ according to a set of training snapshots. It consists of finding an approximation of $\overline{\boldsymbol{r}}(\boldsymbol{\Phi} \cdot \boldsymbol{q})$ by summing the contributions of m elements belonging to a reduced integration domain (RID). The contribution of each element of the RID (indexed e) is weighted by a nonzero positive factor $\xi_e \geq 0$ to match the energy of the full system and ensure positiveness. As a result, the reduced internal forces can be directly approximated in basis $\boldsymbol{\Phi}$ as described in (8):

$$\overline{\boldsymbol{r}}(\boldsymbol{\Phi}\cdot\boldsymbol{q}) \approx \sum_{e\,\in\,\widetilde{\Omega}}^{m} \xi_e \boldsymbol{\Phi}^{\mathrm{T}}\cdot\boldsymbol{L}_{\mathrm{e}}^{\mathrm{T}}\cdot\boldsymbol{r}_e(\boldsymbol{L}_{\mathrm{e}}\cdot\boldsymbol{\Phi}\cdot\boldsymbol{q}) \tag{8}$$

where $\boldsymbol{r}_e(\boldsymbol{L}_{\mathrm{e}}\cdot\boldsymbol{\Phi}\cdot\boldsymbol{q}) \in \mathbb{R}^{N_c}$ is the restoring force vector related to the e^{th} finite element, $\boldsymbol{L}_e \in \mathbb{R}^{N_c \times N_{DOFs}}$ is a collocation matrix used to select the displacements of the nodes connected to the e^{th} finite element, and $\widetilde{\Omega}$ is the reduced set of elements belonging to the RID (9):

$$\widetilde{\Omega} \in \{e \in \{1,\dots,N_e\} \mid \xi_e \geq 0\}. \tag{9}$$

The weighting factors ξ_e are defined according to n_s snapshots of $\boldsymbol{r}^{\mathrm{u}}(\boldsymbol{u}) \in \mathbb{R}^{N_e \cdot N_c}$ computed in the high dimensional full basis, while the displacement basis $\boldsymbol{\Phi}$ is built using snapshots of $\boldsymbol{u} \in \mathbb{R}^{N_{DOFs}}$ as described in Section 2. Contrary to the UDEIM, the ECSW does not require splitting the restoring force vector into linear and nonlinear parts to ensure stability. The balance equation (8) can be written as a matrix system for the n_s snapshots according to (10):

$$\boldsymbol{Y}\cdot\boldsymbol{\xi} = \boldsymbol{b} \quad \text{with} \quad \boldsymbol{b} = \begin{pmatrix} \overline{\boldsymbol{r}}_1 \\ \vdots \\ \overline{\boldsymbol{r}}_{n_s} \end{pmatrix} = \begin{pmatrix} \sum_{e=1}^{N_e} \boldsymbol{\Phi}^{\mathrm{T}}\cdot\boldsymbol{L}_e^{\mathrm{T}}\cdot\boldsymbol{r}_e^{\mathrm{u}}(\boldsymbol{L}_e\cdot\boldsymbol{u}_1) \\ \vdots \\ \sum_{e=1}^{N_e} \boldsymbol{\Phi}^{\mathrm{T}}\cdot\boldsymbol{L}_e^{\mathrm{T}}\cdot\boldsymbol{r}_e^{\mathrm{u}}(\boldsymbol{L}_e\cdot\boldsymbol{u}_{n_s}) \end{pmatrix} \tag{10}$$

where $\boldsymbol{\xi} \in \mathbb{R}^{N_e}$ is a vector containing the weighting factors $\xi_{e\,=\,1,\dots,N_e}$, $\boldsymbol{b} \in \mathbb{R}^{n \cdot n_s}$ is a vector containing the reduced restoring force vectors $\overline{\boldsymbol{r}}_{j\,=\,1,\dots,n_s}$ (10), and $\boldsymbol{Y} \in \mathbb{R}^{n \cdot n_s \times N_e}$ is a matrix containing the contribution of each finite element in the reduced basis $\boldsymbol{\Phi}$ (11):

$$\boldsymbol{Y} = \begin{pmatrix} \boldsymbol{\Phi}^{\mathrm{T}}\cdot\boldsymbol{L}_1^{\mathrm{T}}\cdot\boldsymbol{r}_1^{\mathrm{u}}(\boldsymbol{L}_1\cdot\boldsymbol{u}_1) & \dots & \boldsymbol{\Phi}^{\mathrm{T}}\cdot\boldsymbol{L}_{N_e}^{\mathrm{T}}\cdot\boldsymbol{r}_{N_e}^{\mathrm{u}}(\boldsymbol{L}_{N_e}\cdot\boldsymbol{u}_1) \\ \vdots & \ddots & \vdots \\ \boldsymbol{\Phi}^{\mathrm{T}}\cdot\boldsymbol{L}_1^{\mathrm{T}}\cdot\boldsymbol{r}_1^{\mathrm{u}}(\boldsymbol{L}_1\cdot\boldsymbol{u}_{n_s}) & \dots & \boldsymbol{\Phi}^{\mathrm{T}}\cdot\boldsymbol{L}_{N_e}^{\mathrm{T}}\cdot\boldsymbol{r}_{N_e}^{\mathrm{u}}(\boldsymbol{L}_{N_e}\cdot\boldsymbol{u}_{n_s}) \end{pmatrix}. \tag{11}$$

The matrix system (10) is exactly fulfilled if each finite element is weighed with one, leading to $\boldsymbol{\xi} = (1 \quad \dots \quad 1)^{\mathrm{T}}$ so that all the elements belong to the RID. To achieve a reduction, (10) is approximated up to a tolerance τ with a sparse weighting vector $\boldsymbol{\xi}^* \in \mathbb{R}^{N_e}$ containing as many zero entries as possible. Each entry of $\boldsymbol{\xi}^*$ is constrained to be positive to ensure the positive definiteness of the virtual work. The constrained optimization problem to solve is written in (12):

$$\arg\min \#(e \mid \xi_e^* \neq 0) \quad \text{subject to} \quad \|\boldsymbol{Y}\cdot\boldsymbol{\xi}^* - \boldsymbol{b}\|_2 \leq \tau\|\boldsymbol{b}\|_2 \quad \text{and} \quad \boldsymbol{\xi}^* \geq \boldsymbol{0}. \tag{12}$$

Despite being Nondeterministic Polynomial time (NP) hard to solve, a solution of (12) can be computed using a SNNLS solver as described in Algorithm 2. It uses a greedy method seeking iteratively for a solution fitting the positivity constraint [34]. Note that the matrix $\boldsymbol{Y}_{\widetilde{\Omega}}$ is a submatrix of $\boldsymbol{Y}$ obtained by taking only the columns corresponding to the index set $\widetilde{\Omega}$.

Once the SNNLS problem is solved, the m nonzero positive weighting factors ξ_e^* are used to approximate $\overline{\boldsymbol{r}}(\boldsymbol{\Phi}\cdot\boldsymbol{q})$ (8) according to the reduced set of elements defined in (9). The reduced tangent stiffness matrix $\overline{\boldsymbol{K}}_{\mathrm{T}}$ is computed by derivation of (8) with respect to $\boldsymbol{q}$ as described in (13):

$$\overline{\boldsymbol{K}}_{\mathrm{T}} = \frac{\partial \overline{\boldsymbol{r}}(\boldsymbol{q})}{\partial \boldsymbol{q}} \approx \sum_{e \in \tilde{\Omega}}^{m} \xi_e \boldsymbol{\Phi}^{\mathrm{T}} \cdot \boldsymbol{L}_{\mathrm{e}}^{\mathrm{T}} \cdot \boldsymbol{K}_{\mathrm{T,e}}(\boldsymbol{L}_{\mathrm{e}} \cdot \boldsymbol{\Phi} \cdot \boldsymbol{q}) \cdot \boldsymbol{L}_{\mathrm{e}} \cdot \boldsymbol{\Phi} \tag{13}$$

where $\boldsymbol{K}_{\mathrm{T,e}}(\boldsymbol{L}_{\mathrm{e}} \cdot \boldsymbol{\Phi} \cdot \boldsymbol{q}) \in \mathbb{R}^{N_c \times N_c}$ is the tangent stiffness matrix related to the e^{th} finite element. Contrary to the UDEIM, the ECSW preserves desirable properties like passivity, stability, symmetry, and variational consistency since $\overline{\boldsymbol{K}}_{\mathrm{T}}$ is symmetric. However, its accuracy still depends on the choice of the training dataset for which the equality of the virtual work is enforced. The tolerance τ also depends on the case study since its value is worth between 10^{-4} and 10^{-2} in the literature ([32], [35]).

Algorithm 2: Sparse Non-Negative Least Square (sNNLS) solver.

Input: Matrix $\boldsymbol{Y}$, vector $\boldsymbol{b}$, and tolerance $\tau \in]0,1[$
Output: Index set $\tilde{\Omega}$ and sparse vector $\boldsymbol{\xi}^*$

Initiate the index set of entries where $\xi_e^* > 0$: $\tilde{\Omega} = \{\ \ \}$
Initiate the sparse vector: $\boldsymbol{\xi}^* = \boldsymbol{0}$
Initiate the residual: $\boldsymbol{res} = \boldsymbol{b}$

While $\|\boldsymbol{res}\|_2 > \tau \|\boldsymbol{b}\|_2$
  Compute error measure: $\boldsymbol{\mu} = \boldsymbol{Y}^{\mathrm{T}} \cdot \boldsymbol{res}$
  e = index of the maximum component of $\boldsymbol{\mu}$
  Augment $\tilde{\Omega} = \tilde{\Omega} \cap e$
  Initiate Boolean: $\kappa = True$
  While $\kappa = True$
    Initiate trial solution satisfying the positivity constraint: $\boldsymbol{\zeta} = \boldsymbol{0}$
    Solve on the index set $\tilde{\Omega}$: $\boldsymbol{\zeta}_{\tilde{\Omega}} = (\boldsymbol{Y}_{\tilde{\Omega}})^{+} \cdot \boldsymbol{b}$
    If $\min(\boldsymbol{\zeta}) > 0$
      Positivity constraint fulfilled: $\boldsymbol{\xi}^* = \boldsymbol{\zeta}$
      Update Boolean: $\kappa = False$
    Else
      Define the index set $\tilde{\Pi}$ where the positivity constraint is not fulfilled:
      $\tilde{\Pi} = \{e \in \tilde{\Omega} \mid \zeta_e < 0\}$
      Compute the step width α to set the maximum violation to zero:
      $\alpha = \min\{\xi_e^*/(\xi_e^* - \zeta_e) \mid e < \tilde{\Pi}\}$
      Correct constraint violation: $\boldsymbol{\xi}^* = \boldsymbol{\xi}^* + \alpha(\boldsymbol{\zeta} - \boldsymbol{\xi}^*)$
      Update the index set $\tilde{\Omega}$: $\tilde{\Omega} = \{e \mid \xi_e \neq 0\}$
    End
  Update residual: $\boldsymbol{res} = \boldsymbol{b} - \boldsymbol{Y}_{\tilde{\Omega}} \cdot \boldsymbol{\xi}_{\tilde{\Omega}}^*$
  End
End

The ECSW is compared to the UDEIM in Section 4 in the case of parametric analyses on a RC structure subjected to earthquakes. One online phase was repeated with an increasing number of elements in the RID. Analyses about the properties of the external loading (e.g., earthquakes) and material properties were carried out.

4 APPLICATIONS

4.1 Numerical modeling of RC structure

The global kinematics of the case study was modeled using Timoshenko multi-fiber beam elements (see Figure 1) defined by quadratic and cubic shape functions [36].

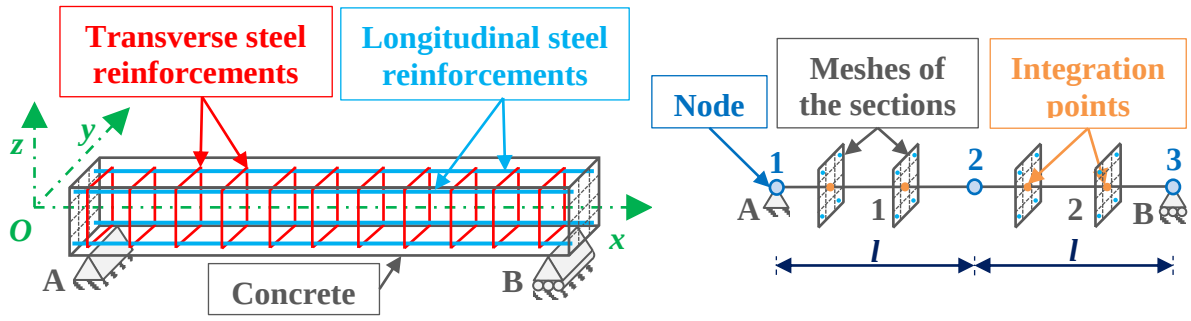

(a) (b)

Figure 1: Simply supported reinforced concrete beam (a), and multifibre mesh with two Timoshenko beam elements (b).

Knowing that the length/height ratio of the structural components (e.g., beams, or columns) is usually higher than 10 in civil engineering structures, the damage was assumed to be mainly due to bending. A "unilateral" damage law with frictional sliding developed to model quasi-brittle materials under dynamic or cyclic loadings [37] was used for concrete fibers (see Figure 2 (a) & (b)), while the steel rebars were modeled using a bilinear elastic-plastic law (see Figure 2 (c)).

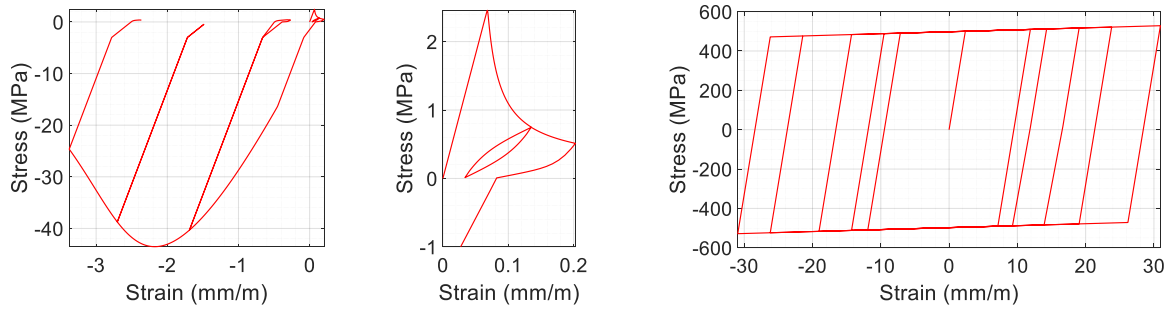

(a) (b) (c)

Figure 2: Uniaxial damage law for concrete with opening/closing of cracks (a) and frictional sliding (b), and uniaxial bilinear elastic-plastic law with kinematic hardening for steel rebars subjected to cyclic loadings (c).

4.2 Case study

The case study was a L-shaped three-story reinforced concrete building defined by 2383 nodes linked by 2866 multifibre beam elements (see Figure 3 (a)). All the columns were embedded to the floor level, and 14292 free DOFs modeled the structure. All stories were 3 m high, and each span was 3 m long. Two stairwells occupying areas of 2 × 2 m² were located at the ends of the building. Both were modeled by adding three columns to locally increase the stiffness. A mass per unit area of 400 kg/m² was applied to both floors via the longitudinal beams, whereas the masses of the stairwells were neglected.

The columns had a 15 × 15 cm square cross-section, and the beams had a 15 × 25 cm rectangular one. The diameter of each longitudinal steel rebar was set at 12 mm, and the steel coating was 20 mm (*cf.* Figure 3 (b)). The cross-sections of beams and columns were divided into 3 × 5 and 3 × 3 surface elements, respectively. The concrete fibers were located at the integration points of the surface elements (grey dots), while the steel fibers (blue dots) were located at 34 mm from the corners of the cross-sections (*cf.* Figure 3 (c)).

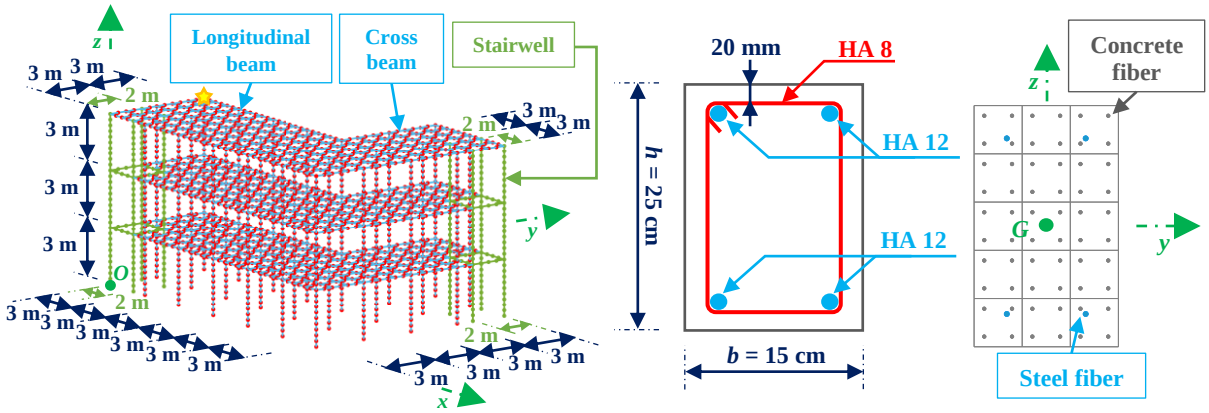

(a) (b) (c)

Figure 3: Mesh of the building (a), cross-section of the beams (b), and mesh of the cross-section of the beams (c).

The main eigenmodes and percentages of effective modal mass are summarized in Table 1. The structure weighed 255 tons and was mainly affected by the six first eigenmodes along the ***x*** and ***y***-axes, with a cumulative modal mass reaching 253 tons (i.e., 99.6 % of the total mass). A Rayleigh viscous damping ratio modeled the structural damping due to the viscosity of air and materials as well as discontinuities at junctions with respect to this frequency range. It was set at ξ = 2 % at f_1 = 1.10 Hz (first eigenfrequency) and f_6 = 3.96 Hz (sixth eigenfrequency) so that its value reached a minimum around the main eigenmodes [38]. To induce torsional effects at floor level, 0.50 in the x-direction, 0.87 in the y-direction, and 0.30 in the z-direction weighed the ground motions. The dead and live loads were applied statically before entering the time step loop.

Eigenfrequency	% of effective modal mass		
(Hz)	***x***-axis	***y***-axis	***z***-axis
1.10	17.5	71.6	~ 0
1.11	72.6	18.3	~ 0
1.38	1.15	1.10	~ 0
3.15	1.08	7.35	~ 0
3.18	7.29	1.05	~ 0
3.96	0.09	0.12	~ 0

Table 1: Main eigenfrequencies and percentages of effective modal mass of the model.

4.3 Vulnerability analysis involving several ground motions

The POD-UDEIM and the POD-ECSW hyper-reduced order modeling (HROM) methods were applied to compute the response of the L-shaped three-story building under earthquake

conditions. Several natural ground motions fitting the design spectrum of the "Rhonetal" microzoning area around Visp in Switzerland (available here) modeled the seismic hazard. POD-UDEIM and POD-ECSW HROMs were first built according to 3088 snapshots based on the full order model (FOM) responses related to the ground motions in Figure 4 (a) & (b). Both HROMS were then used to approximate the response related to the ground motion in Figure 4 (c). All signals were of the same order of magnitude (with peak ground acceleration between 2.4 m/s² and 2.6 m/s²) and sampled at 100 Hz. Still, their frequency, strong motion duration, and number of aftershocks differed.

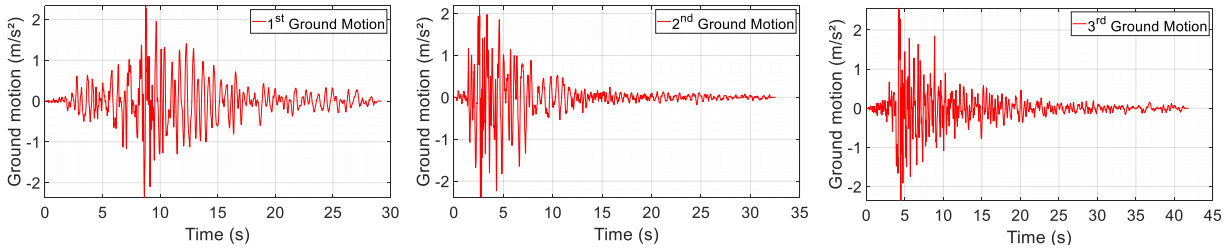

Figure 4: Ground motions used to compute snapshots (a) & (b), and ground motion used to approximate the response of the building using HROMS (c).

The displacement component u_x of the northwest corner (see yellow star in Figure 3 (a)) is plotted in Figure 5 for each ground motion. All calculations were carried out on an Intel® Core™ i9-10900K CPU @ 3.70 GHz and 64 GB RAM personal computer using custom procedures implemented in MATLAB© software. The FEM analyses were performed using an implicit Newmark method ($\beta = 0.25$ and $\gamma = 0.50$) with a time step Δt equal to 10 ms. A relative tolerance of 10^{-6} controlled the convergence of the Newton-Raphson algorithm. Results show that both responses were highly affected in amplitude and frequency by the material nonlinearities.

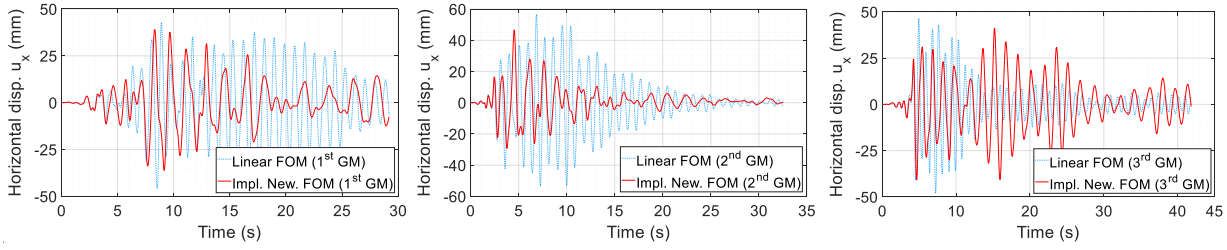

Figure 5: Displacement component u_x of the northwest corner related to the 1st (a), 2nd (b), and 3rd (c) ground motions.

The snapshots used to build the HROMs were selected every two-time steps (i.e., every 20 ms) to avoid redundancy of the input data. As a result, 1460 snapshots were related to the first ground motion, and 1628 to the second.

A SVD was performed on the displacement snapshots to build the modal basis $\boldsymbol{\Phi}$. A number n of 35 POD modes fulfilled the criterion (1) considering a tolerance ε equal to 10^{-2} [15] (see Figure 6 (a)). The three main POD modes drawn in Figure 6 (b), (c), and (d) show that bending and torsion mainly affect the nonlinear response of the L-shaped three-story building. The first POD mode ($R_1 = 1.15$ Hz) is close to the first eigenmodes of bending along the $\boldsymbol{x}$ and $\boldsymbol{y}$-axes ($f_1 = 1.10$ Hz and $f_2 = 1.11$ Hz). The second ($R_2 = 3.31$ Hz) refers to the second eigenmodes of

bending along the ***x*** and ***y***-axes (f_4 = 3.15 Hz and f_5 = 3.18 Hz). The third (R_3 = 2.08 Hz) models torsional effects about the ***z***-axis and could be compared to the third eigenmode (f_3 = 1.38 Hz).

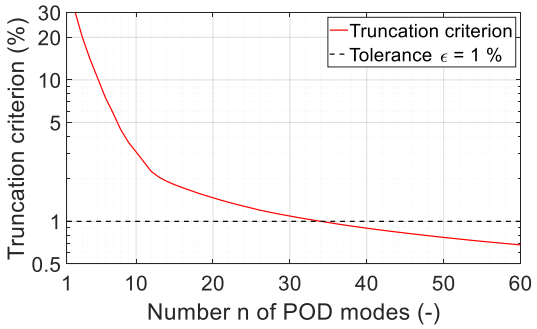

(a)

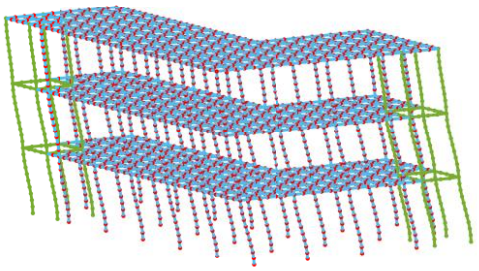

R_1 = 1.15 Hz

(b)

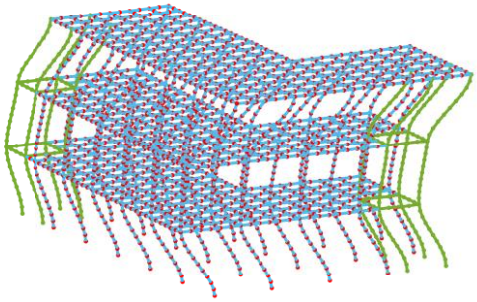

R_2 = 3.31 Hz

(c)

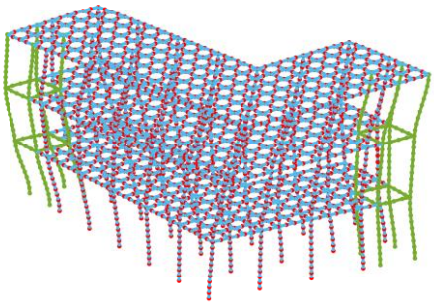

R_3 = 2.08 Hz

(d)

Figure 6: Criterion used to truncate the POD modal basis (a), and shapes and Rayleigh quotients of the first (b), second (c), and third (d) POD modes.

Knowing that the efficiency of UDEIM and ECSW hyper-reduction procedures highly depends on the snapshots, the nonlinear material laws, and the number m of element in the RID, a sensitivity analysis compares the accuracy of both methods with a value of m between 50 and 1000. The online and offline CPU times, the error, and the number of iterations in Figure 7 quantify the reliability of the HROMs to compute the nonlinear response related to the third ground motion. The solutions $(\boldsymbol{u}, \boldsymbol{r})$ are compared to the FOM $(\boldsymbol{u}^{\mathrm{FOM}}, \boldsymbol{r}^{\mathrm{FOM}})$ using the strain energy error $\varepsilon_{\mathrm{Ed}}$ defined in (14):

$$\varepsilon_{\mathrm{E_d}} = \frac{\|\Delta E_{\mathrm{d}}\|}{\left\|E_{\mathrm{d}}^{\mathrm{FOM}}\right\|} 100\ \% \quad \text{with} \quad \|\Delta E_{\mathrm{d}}\| = \frac{1}{2N_t \Delta t} \int_0^{N_t \cdot \Delta t} \left|\boldsymbol{\Delta u}^{\mathrm{T}}(t) \cdot \boldsymbol{\Delta r}(t)\right| dt \tag{14}$$

where $E_{\mathrm{d}}^{\mathrm{FOM}}$ is the strain energy of the implicit Newmark FOM, ΔE_{d} is the difference in strain energy, N_t is the number of time intervals, Δt is the time step, $\boldsymbol{\Delta u} = \boldsymbol{u} - \boldsymbol{u}^{\mathrm{FOM}}$ is the difference in displacements, and $\boldsymbol{\Delta r} = \boldsymbol{r} - \boldsymbol{r}^{\mathrm{FOM}}$ is the difference in restoring forces.

Errors in Figure 7 (a) show that the POD-UDEIM is more accurate than the POD-ECSW when the RID is less than 250 elements since only the nonlinear part of the restoring forces are approximated. This is clearly visible in Figure 8 (a) where only 100 elements are required to ensure that the displacement component u_x of the northwest corner agrees well in frequency with the FOM, while at least 200 are necessary with the POD-ECSW (see Figure 8 (b)). However, the later becomes more efficient when new elements are added to the RID, leading to a residual error approximately equal to 0.15 % when m is higher than 350. This value is twice as

high with the POD-UDEIM as it stabilizes at 0.32 %. Knowing that the error is equal to 0.12 % with the POD reduced order model, the POD-ECSW is almost as accurate in the present case study.

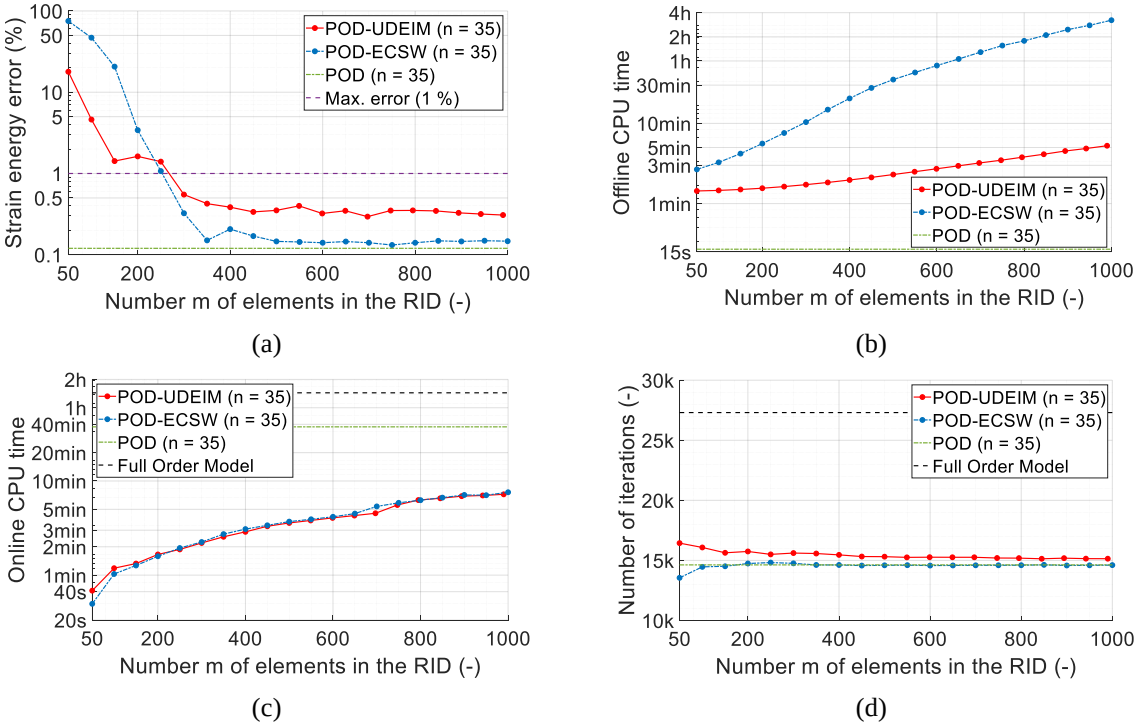

Figure 7: Strain energy error (a), offline CPU time (b), online CPU time (c), and number of iterations (d) with respect to the number of elements in the RID (comparison using the third ground motion with 35 POD modes).

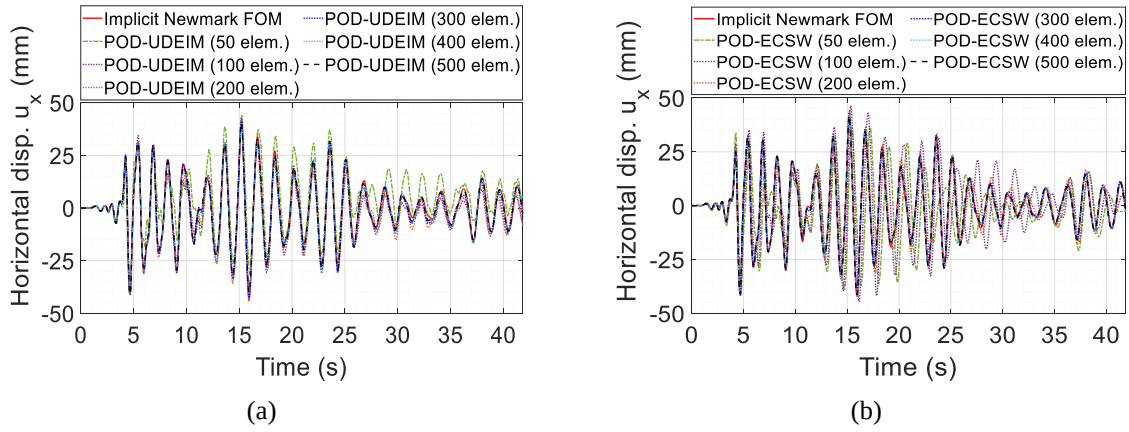

Figure 8: Displacement component u_x of the northwest corner computed with the third ground motion using POD-UDEIM (a) and POD-ECSW (b) HROMs (with 35 POD modes).

Unfortunately, Figure 7 (b) shows that the ECSW is limited since the computational cost of the SNNLS solver ensuring the positivity of the weighting factors (see Algorithm 2) increases drastically with respect to the number m of elements. In comparison, the DEIM algorithm (see Algorithm 1) runs faster considering that it involves only one iterative loop, and that unused components can be added *a posteriori* (as explained in Section 2). As a result, the time necessary to build a RID including 350 elements (i.e., when the residual error is reached) is 8 times

higher with the ECSW (lasting 16 min) than with the UDEIM (lasting 2 min). The POD-ECSW is thus more efficient than the POD-UDEIM provided that the HROM accelerates a large number of FEM analyses (i.e., online phases).

The online CPU times in Figure 7 (c) show that the speed-up factor is approximately the same with both methods, as well as the number of iterations required to solve the problem (see Figure 7 (d)). Using HROMs with a RID including 350 elements allows computing accurately the response of the building in 2 min 45 s, which is 13.8 and 31.6 times faster compared to the POD (~ 38 min) and to the FOM (~ 1 h 27 min), respectively. In addition, less iterations are required when using reduced or hyper-reduced order models since the nonlinearities are directly taken into account in the shape of the POD modes, which further decreases the CPU time. Knowing that it is necessary to iterate 27 k times to solve the equation of motion using the FOM, the number of iterations is approximately 1.7 times lower using the ROMs, with a value that does not exceed 16 k (see Figure 7 (c)). The number of iterations is the same with the POD and the POD-ECSW (~ 14.6 k) but its value slightly increases with the POD-UDEIM (~ 15.2 k) since the approximated tangent stiffness matrix is not fully symmetric, as explained in Section 1.

RIDs including 350 elements built using the UDEIM and the ECSW hyper-reduction methods are drawn in Figure 9 (b) & (c), respectively. Both are compared to the maximal damage index distribution related to the third earthquake (see Figure 9 (a)).

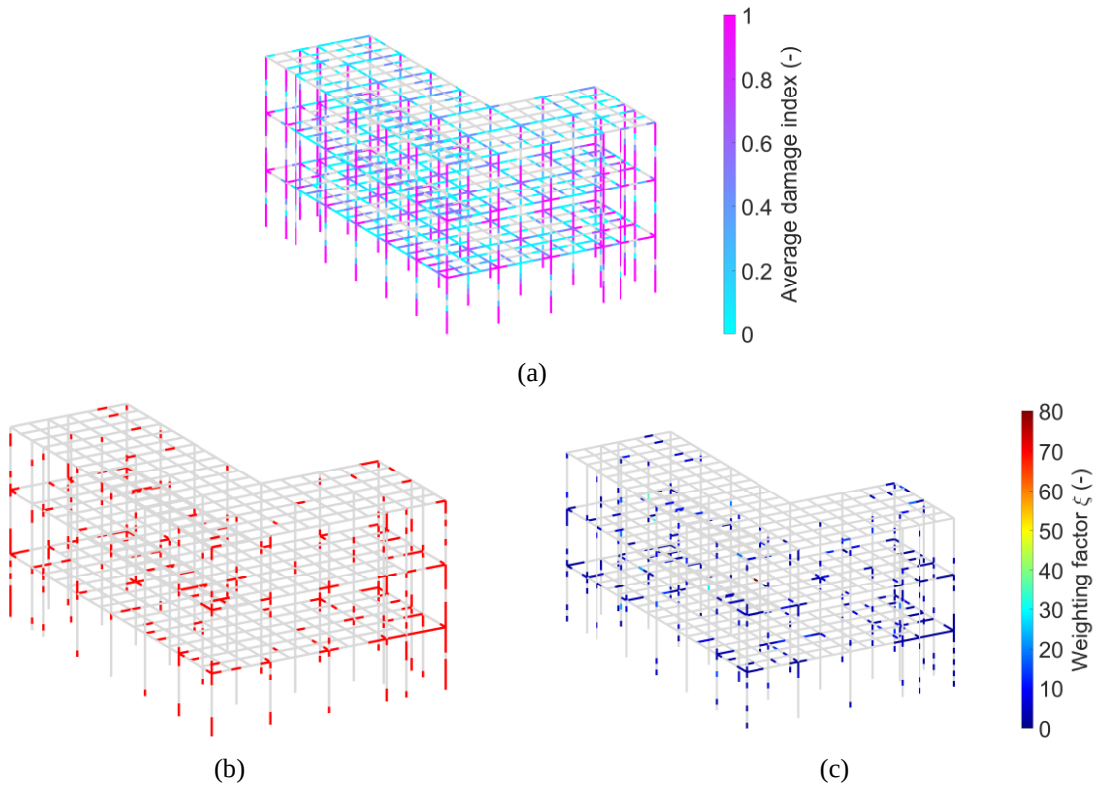

Figure 9: Damage index distribution on the FOM with the third earthquake (1845 damaged beam elements) (a), and RIDs with 35 POD modes and 350 elements: UDEIM (b) and ECSW with weighting factors (c).

In the present case study, 19 % of the 1845 elements where damage appears (i.e., 69 % of the whole structure) are required to correctly approximate the restoring force vector during the online phase. Many of them are located close to the stairwells, where the stiffness increases locally (see the colored elements in Figure 9 (b) and Figure 9 (c)). This shows that both hyper-

reduction methods can approximate strong nonlinearities (e.g., damage) distributed on a large number of elements, as it is commonly the case in the earthquake engineering framework.

4.4 Vulnerability analysis about the material properties

In Section 4.3, the POD-UDEIM and the POD-ECSW hyper-reduction methods proved their efficiency in accelerating vulnerability analyses involving several ground motions. Both methods were next applied to a parametric analysis about the concrete properties under earthquake conditions. The dynamic response related to the ground motion in Figure 10 (a) was computed considering that three different concretes can be used to model the L-shaped three-story building (see Figure 10 (b) & (c)). Table 2 gives the elastic modulus E, the tensile strength f_t, and the compressive strength f_c of each one of them.

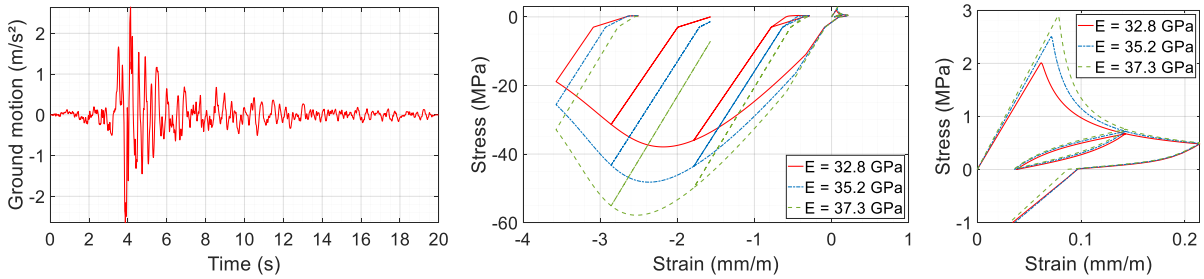

Figure 10: Ground motion used for the parametric analysis (a), uniaxial damage laws for each concrete with opening/closing of cracks (b), and frictional sliding (c).

Concrete # (-)	E (GPa)	f_t (MPa)	f_c (MPa)
1	32.8	2.0	38.0
2	35.2	2.5	48.0
3	37.3	2.9	58.0

Table 2: Properties of the concretes used in the parametric analysis.

A set of 3000 snapshots was built using the first and third concretes responses, defined by elastic modules of 32.8 GPa and 37.3 GPa, respectively. The response of the second, defined by an elastic modulus of 35.2 GPa, was then approximated using HROMs. The displacement component u_x plotted in Figure 11 (a) shows that the higher the tensile strength, the higher the energy dissipated by frictional sliding. As a result, differences in amplitude and frequency appear as damage increases.

The snapshots were selected every two-time steps (i.e., every 20 ms) from the results of dynamic analyses related to the ground motion in Figure 10 (a). A set of 1000 snapshots also came from the results of static analyses to be sure that the reduced order model was able to apply the dead and the live loads before entering the time step loop regardless of the concrete properties. According to Figure 11 (b), a basis $\boldsymbol{\Phi}$ of 20 POD modes fulfills the criterion (1) when a tolerance of 1 % is used.

The error and the online CPU times in Figure 12 (a) & (c) quantify the efficiency of the POD-UDEIM and the POD-ECSW to approximate the nonlinear response of the L-shaped three-story building in the case the second concrete is used. Each online phase includes a static analysis that apply the dead and the live loads using a POD ROM, and a dynamic analysis that

models the effects of the earthquake using HROMs. As in Section 4.3, both methods are compared with respect to the number m of elements in the RID. Results shows that the POD-ECSW is very accurate since only 175 elements are required to reach an error close to 0.30 %. The response of the building (see Figure 12 (d)) can thus be accurately computed in 2 min 15 s, which is 8.4 and 24.0 times faster compared to the POD reduced order model (~ 19 min) and to the FOM (~ 55 min), respectively.

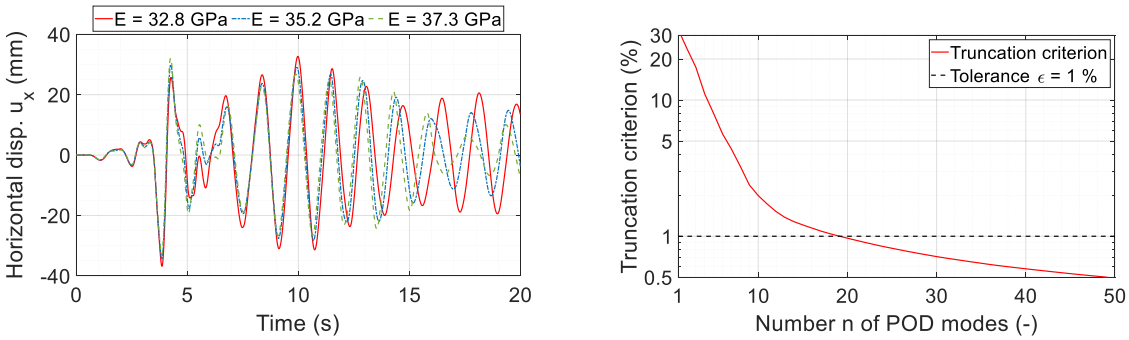

(a) (b)

Figure 11: Displacement component u_x of the northwest corner computed using the FOMs (a), and criterion used to truncate the POD modal basis used to perform the parametric analysis (b).

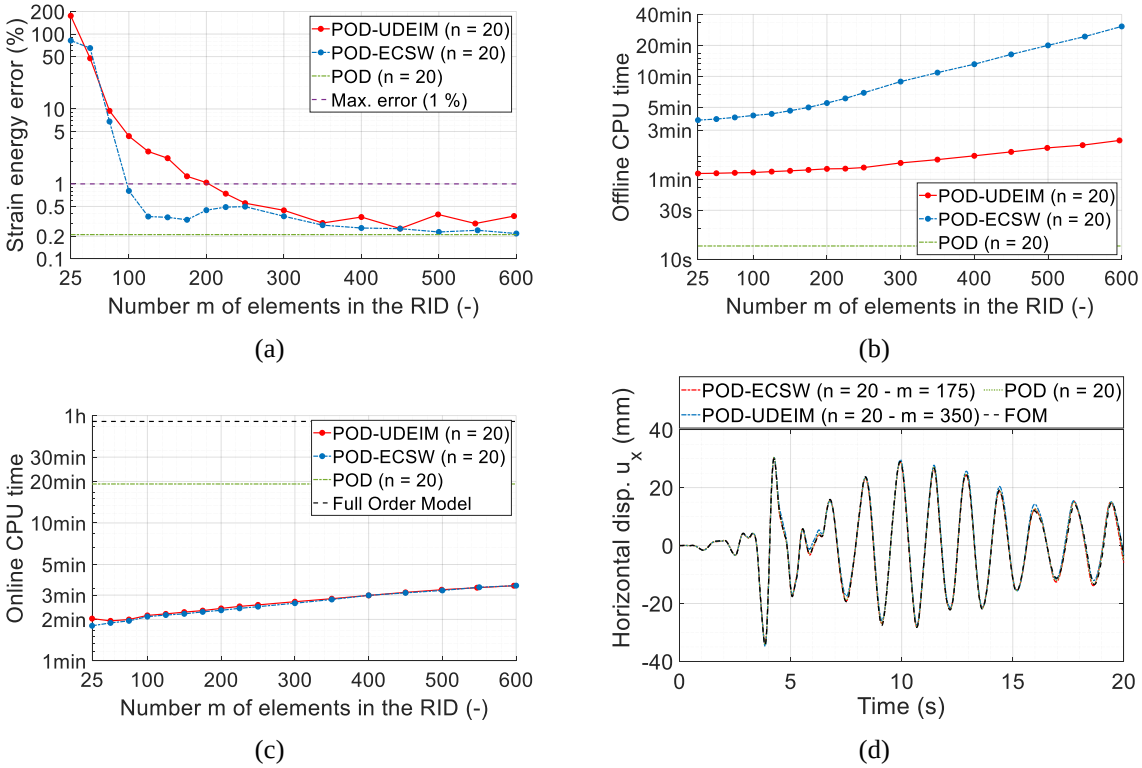

(a) (b)

(c) (d)

Figure 12: Strain energy error (a), offline CPU time (b), online CPU time (c), and displacement u_x of the northwest corner when the residual error is reached (d) (comparison using the second concrete with 20 POD modes).

The POD-UDEIM is less efficient since 350 elements are necessary to guarantee the same residual error, leading to an online CPU time of 2 min 47 s. As a result, the online speed-up factors are lower, with values equal to 6.9 (POD) and 20.2 (FOM). The error stabilizes well with both methods even if slight variations may appear since time-dependent internal variables

are involved. Note that the offline CPU time of the POD-ECSW (m = 175) is 3.2 times higher compared to the POD-UDEIM (m = 350) in the present case study (see Figure 12 (b)). Still, the hyper-reduction method needs to be chosen wisely according to the number of online phases required to complete the parametric analysis, as suggested in Section 4.3.

The damage index distribution in Figure 13 (a) shows that nonlinearities appear in 1673 beam elements (i.e., 58 % of the whole structure) according to the FOM response. The RID achieving the residual error is thus 4.8 and 9.6 times smaller using the UDEIM and the ECSW, respectively (see Figure 13 (b) & (c)). As in Section 4.3, both methods are thus able to approximate solutions in the case damage appears on a large number of elements, making them suitable for analyses using the concrete properties as parameters.

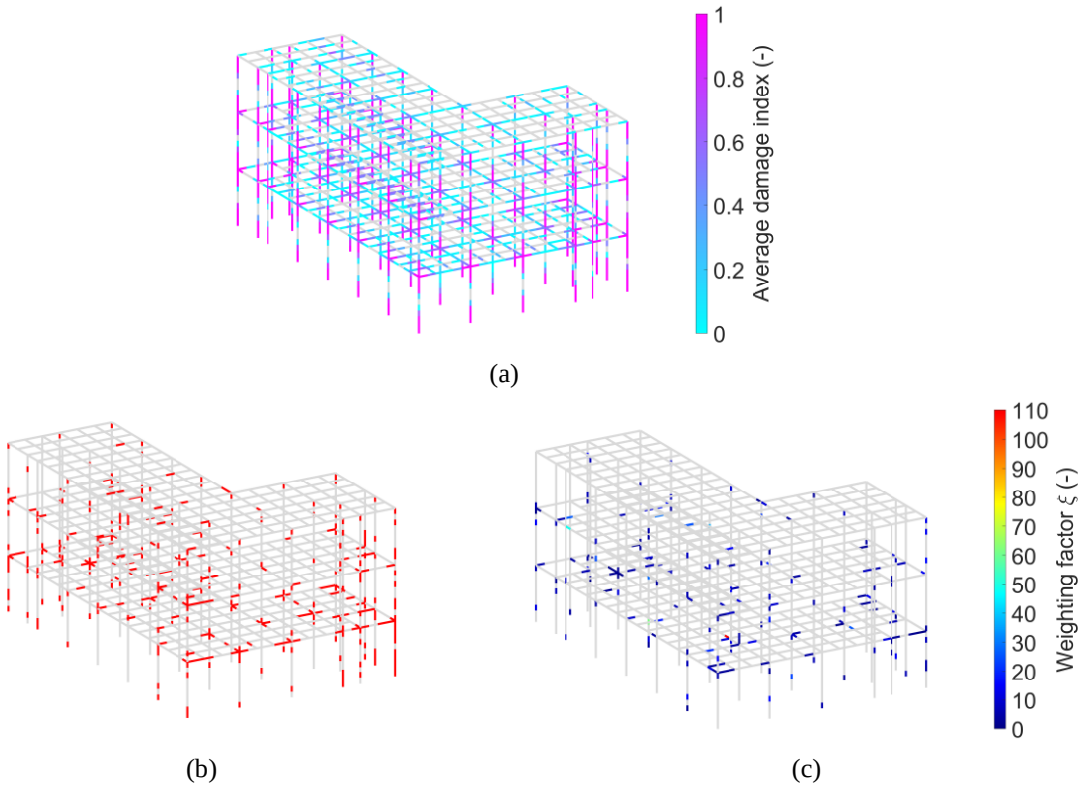

Figure 13: Damage index distribution of the FOM using the second concrete (1673 damaged beam elements) (a), and RIDs with 20 POD modes: UDEIM with 350 elements (b) and ECSW with 175 elements (c).

5 CONCLUSIONS

This paper compared the efficiency of two data-driven hyper-reduced order modeling methods, the POD-UDEIM and the POD-ECSW, to accelerate vulnerability analyses on reinforced concrete structures subjected to earthquakes. Both methods were applied to parametric analyses about the ground motions and the concrete properties. Applications on a L-shaped three-story building made of multi-fiber beam elements showed that both methods can successfully approximate solutions in the case damage appears on a large number of elements. Using HROMs made it possible to perform online FEM analyses from 20 and 32 times faster with errors lower than 0.5 %. The POD-ECSW revealed to be more efficient than the POD-UDEIM during the online phases, allowing for smaller errors, online CPU times, and reduced integration domains. However, the computational cost of the SNNLs solver used during the offline phase remains significantly higher than the DEIM algorithm, especially with high dimensional systems. As a

result, the POD-ECSW saves more CPU time only if the number of online FEM analyses is high enough.

Despite RIDs 5 to 10 times smaller than the high dimensional systems, both methods proved accurate enough to correctly model strong distributed nonlinearities (e.g., damage) involving time-dependent internal variables. Their reliability when applied to vulnerability analyses (e.g., fragility curves) involving earthquakes of differing orders of magnitude (e.g., with peak ground acceleration ranging from 0.5 m/s² to 7 m/s²) is still an open question. Additionally, extending the method to structures modeled by multilayer shells is relevant since these elements are commonly used to model slabs and walls in the earthquake engineering framework. Sensitivity or stochastic analyses about the dimensions (e.g., area of the sections) could also be achieved using HROMs.

REFERENCES

[1] Saidi M., Sozen M. A. Simple nonlinear seismic analysis of R/C structures. *J. Struct. Div., ASCE, 107(5),* 937-52, 1981.

[2] Kilar V., Fazfar P. Simple push-over analysis for asymmetric buildings. *Earthquake Engng. Struct. Dyn., 26,* 233-49, 1997.

[3] Nakashima M., Kato H., Takaoka E. Development of real-time pseudo dynamic testing. *Earthquake Engineering and Structural Dynamics 21(1),* 79-92, 1992.

[4] Moutoussamy L. (2013). Essais hybrides en temps réel sur structures de Génie Civil. *ENS Cachan Phd-thesis,* 2013.

[5] Kosambi D. D. Statistics in function space. *Journal of Indian Mathematical Society 7,* 76-88, 1943.

[6] Karhunen K. Über lineare Methoden in der Wahrscheinlichkeitsrechnung. *Annals of Academic Science Fennicae, Series A1 Mathematics and Physics 37,* 3-79, 1946.

[7] Loève M. Fonctions aléatoires du second ordre. Processus Stochastiques et Mouvement Brownien, 1948.

[8] Sirovich L. Turbulence and the dynamics of coherent structures. I. Coherent structures. *Quarterly of applied mathematics 45.3,* 561-571, 1987.

[9] Hall K. C., Thomas J. P., Dowell E. H. Proper orthogonal decomposition technique for transonic unsteady aerodynamic flows. *AIAA Journal 38.10,* 1853-1862, 2000.

[10] Epureanu B. A parametric analysis of reduced order models of viscous flows in turbomachinery. *Journal of fluids and structures 17.7,* 971-982, 2003.

[11] Ravindran S. S. A reduced-order approach for optimal control of fluids using proper orthogonal decomposition. *International journal for numerical methods in fluids 34.5,* 425-448, 2000.

[12] De Boe P., Golinval J.-C. Principal component analysis of a piezosensor array for damage localization. *Structural health monitoring 2.2,* 137-144, 2003.

[13] Hemez F. M., Doebling S. W. Review and assessment of model updating for non-linear, transient dynamics. *Mechanical Systems and Signal Processing 15.1,* 45-74, 2001.

[14] Azeez M. F. A., Vakakis A. F. Numerical and experimental analysis of a continuous overhung rotor undergoing vibro-impacts. *International journal of non-linear mechanics 34.3*, 415-435, 1999.

[15] Ayoub N., Deü J.-F., Larbi W., Pais J., Rouleau L. Application of the POD method to nonlinear dynamic analysis of reinforced concrete frame structures subjected to earthquakes, *Engineering Structures, 270*, 114854 (9 pages), 2022.

[16] Chaturantabut S., Sorensen D.C. Nonlinear model reduction via discrete empirical interpolation. *SIAM J. Sci. Comput. 32 (5)*, 2737-2764, 2010.

[17] Everson R., Sirovich L. Karhunen-Loève procedure for gappy data. *Journal of the Optical Society of America A 12.8*, 1657-1664, 1995.

[18] Bui-Thanh T., Damodaran M., Willcox K. Proper orthogonal decomposition extensions for parametric applications in compressible aerodynamics. *AIAA paper 4213*, 2003.

[19] Willcox K. Unsteady flow sensing and estimation via the gappy proper orthogonal decomposition. *Computers & fluids 35.2*, 208-226, 2006.

[20] Astrid P. Reduction of process simulation models: a proper orthogonal decomposition approach. *Technische Universiteit Eindhoven PhD-thesis*, 2004.

[21] Rutzmoser J. B. Model order reduction for nonlinear structural dynamics: simulation-free approaches. *Technischen Universität München PhD-thesis*, 2017.

[22] Tiso P., Rixen D. J. Discrete empirical interpolation method for finite element structural dynamics. *Nonlinear Modelling and Applications, Volume 2. Springer*, 53-65, 2013.

[23] Peherstorfer B., Butnaru D., Willcox K., Bungartz H.-J. Localized discrete empirical interpolation method. *SIAM Journal on Scientific Computing 36.1, A168-A192*, 2014.

[24] Ghavamian F., Tiso P., Simone A. POD-DEIM model order reduction for strain-softening viscoplasticity. *Comput. Methods Appl. Mech. Engrg. 317*, 458-479, 2017.

[25] Antil H., Heinkenschloss M., Sorensen D. C. Application of the discrete empirical interpolation method to reduced order modeling of nonlinear and parametric systems. *Reduced order methods for modeling and computational reduction. Springer*, 101-136, 2014.

[26] Benner P., Gugercin S., Willcox K. A Survey of Projection-based Model Reduction Methods for Parametric Dynamical Systems. *SIAM Review 57.4*, 483-531, 2015.

[27] Drmac Z., Gugercin S. A new selection operator for the discrete empirical interpolation method - Improved a priori error bound and extensions. *SIAM Journal on Scientific Computing 38.2*, A631-A634, 2016.

[28] Radermacher A., Reese S. POD-based model reduction with empirical interpolation applied to nonlinear elasticity. *International Journal for Numerical Methods in Engineering 107.6*, 425-448, 2016.

[29] An S. S., Kim T., James D. L. Optimizing cubature for efficient integration of subspace deformations. *ACM Transactions on Graphics (TOG) 27.5*, No. 165, 2008.

[30] Farhat C., Avery P., Chapman T., Cortial J. Dimensional reduction of nonlinear finite element dynamic models with finite rotations and energy-based mesh sampling and weighting for computational efficiency. *International Journal for Numerical Methods in Engineering 98*, 625-662, 2014.

[31] Farhat C., Chapman T., Avery P. Structure-preserving, stability, and accuracy properties of the energy-conserving sampling and weighting method for the hyper reduction of nonlinear finite element dynamics models. *International Journal for Numerical Methods in Engineering 102.5*, 1077-1110, 2015.

[32] Chapman T., Avery P., Collins P, Farhat C. Accelerated mesh sampling for the hyper reduction of nonlinear computational models. *International Journal for Numerical Methods in Engineering 109.12*, 1623-1654, 2017.

[33] Hernandez J. A., Caicedo M. A., Ferrer A. Dimensional hyper-reduction of nonlinear finite element models via empirical cubature. *Computer Methods in Applied Mechanics and Engineering 313*, 687-722, 2017.

[34] Lawson C. L., Hanson R. J. Solving least square problems. Vol. 15. *SIAM*, 1995.

[35] Farhat C., Chapman T., Avery P. ECSW: An energy-based structure-preserving method for the hyper reduction of nonlinear finite element reduced-order models. *International Journal for Numerical Methods in Engineering 00*, 1-33, 2013.

[36] Davenne L., Ragueneau F., Mazars J., Ibrahimbegovic A. Efficient approaches to finite element analysis in earthquake engineering. *Computers and Structures 81*, 1223–1239, 2003.

[37] Richard B., Ragueneau F. Continuum damage mechanics based model for quasi brittle materials subjected to cyclic loadings: Formulations, numerical implementation and applications. Engineering Fracture Mechanics 98, 383-406, 2013.

[38] Chambreuil C. Modelling of damping in nonlinear dynamic analyses of reinforced concrete structures: constitutive formulations and experimental identification. ENS Paris-Saclay PhD-thesis, 2022.

[39] https://www.vs.ch/documents/315040/2787090/Karte_MSS_Visp.pdf/b52cae9a-a1bf-4b19-922c-1d0bfc080b1b